Article

Modulating the Primary and Secondary Coordination Spheres of Single Ni(II) Sites in Metal−Organic Frameworks for Boosting Photocatalysis

Ge Yang,[⊥] Denan Wang,[⊥] Yang Wang,[⊥] Wenhui Hu, Shuaishuai Hu, Jun Jiang, Jier Huang,* and Hai-Long Jiang*

Read Online

ACCESS | Metrics & More | Article Recommendations | Supporting Information

ABSTRACT: Though the coordination environment of single metal sites has been recognized to be of great importance in promoting catalysis, the influence of simultaneous precise modulation of primary and secondary coordination spheres on catalysis remains largely unknown. Herein, a series of single Ni(II) sites with altered primary and secondary coordination spheres have been installed onto metal−organic frameworks (MOFs) with UiO-67 skeleton, affording UiO−Ni−X−Y (X = S, O; Y = H, Cl, CF$_3$) with X and Y on the primary and secondary coordination spheres, respectively. Upon deposition with CdS nanoparticles, the resulting composites present high photocatalytic H$_2$ production rates, in which the optimized CdS/UiO−Ni−S−CF$_3$ exhibits an excellent activity of 13.44 mmol g^{-1}, ∼500 folds of the pristine catalyst (29.6 μmol g^{-1} for CdS/UiO), in 8 h, highlighting the key role of microenvironment modulation around Ni sites. Charge kinetic analysis and theoretical calculation results demonstrate that the charge transfer dynamics and reaction energy barrier are closely correlated with their coordination spheres. This work manifests the advantages of MOFs in the fabrication of structurally precise catalysts and the elucidation of particular influences of microenvironment modulation around single metal sites on the catalytic performance.
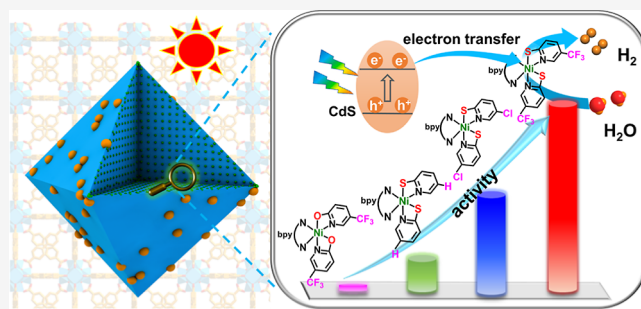
INTRODUCTION

With the scarcity of energy resources, the pursuit of renewable and clean energy sources has become imperative. The conversion of sustainable solar energy into hydrogen as a secondary source has emerged as a promising and environmentally friendly technology.[1−3] The development of low-cost photocatalysts with atomic precision, which promote charge separation for efficient hydrogen production, continues to be a significant challenge and a long-term objective.[4−6] In recent years, nickel, a base metal, has gained recognition as a promising candidate for photocatalytic H$_2$ production due to its easily accessible oxidation states.[7−9] Inspired by the {NiFe} hydrogenases, a range of nickel complexes with rationally designed ligands have been developed to endow Ni(II) centers with excellent photocatalytic performance.[9] Nevertheless, replicating the catalytic metal sites of hydrogen-producing metalloenzymes is insufficient for gaining a comprehensive understanding of the catalytic mechanism and the relationship between structure and activity. The unique physicochemical microenvironment surrounding catalytic metal sites in enzymes plays crucial roles in catalysis; their synergistic functions in the binding pocket are responsible for the remarkable activity and selectivity endowed by enzymes.[10−12] Inspired by enzymes, precise microenvironment modulation around single metal sites is of great importance. Although there have been a number of reports on coordination environment modulation of single metal sites for boosting catalytic activity and selectivity,[13−16] studies on the secondary coordination effect influencing catalysis remain relatively rare and are almost limited to homogeneous catalysts.[17−19] Furthermore, the simultaneous manipulation of both primary and secondary coordination spheres around catalytic metal sites would largely regulate their catalytic performance; unfortunately, this remains a grand challenge for heterogeneous catalysts that are preferable toward practical applications due to the ease of recyclability.[20,21] Therefore, it is highly desirable to find ideal heterogeneous catalysts that can achieve atomically precise microenvironment modulation surrounding catalytic metal sites, which will not only optimize the catalytic performance but also facilitate the understanding of the corresponding intrinsic mechanism.
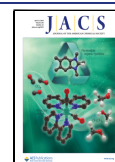
Taking into account the above considerations, metal–organic frameworks (MOFs), would be an ideal platform to fulfill the aforementioned requirements thanks to their well-defined and tailorable structures.[22−27] Remarkable progress has been made to improve catalytic performance via structural modification of MOFs,[28−32] especially incorporating single metal sites into MOFs to promote charge separation for efficient photocatalysis.[29] There have also been quite a few studies on modulating the primary coordination sphere of single metal sites in MOFs.[33−35] However, to the best of our knowledge, the simultaneous modulation of primary and secondary coordination spheres of single metal sites in MOFs for boosting photocatalysis remains undeveloped.

In this work, a representative stable MOF with a classical UiO-67 skeleton is assembled by Zr-oxo clusters and 2,2′-bipyridine-5,5′-dicarboxylic acid. The CdS nanoparticles (NPs, 27 ± 0.3 nm) are then decorated on the MOF surface as the photosensitizer to afford the CdS/UiO composite. Subsequently, the chelating N sites on the MOF linker can install single Ni(II) sites that are further six-coordinated by different molecules and feature a well-tailored microenvironment, giving CdS/UiO−Ni−X−Y (X = S, O; Y = H, Cl, CF$_3$) with X and Y on the primary or secondary coordination spheres, respectively (Scheme 1). It is remarkable that regulation of both the

Scheme 1. Schematic Illustration Showing the Synthetic of CdS/UiO−Ni−X−Y (X = S, O; Y = H, Cl, CF$_3$) Composites with Modulated Primary and Secondary Coordination Spheres (Shown as X and Y, Respectively) for Photocatalytic H$_2$ Production
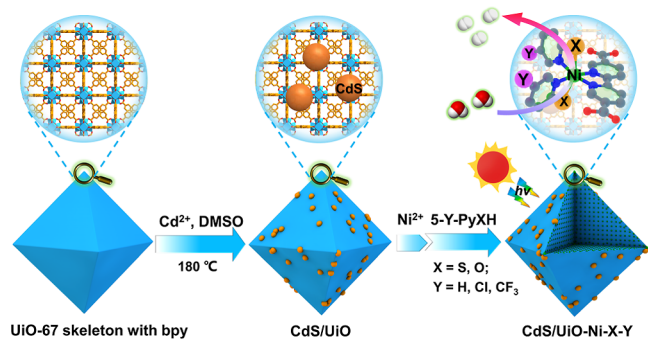
primary and secondary coordination spheres significantly improves the activity. Among the investigated composites, the optimized CdS/UiO−Ni−S−CF$_3$ exhibits an H$_2$ production rate up to 13.44 mmol g^{-1} in 8 h, which is 19 times higher than CdS/UiO−Ni−O−CF$_3$ (0.71 mmol g^{-1}, altered primary coordination sphere) and 4.7 times higher than CdS/UiO−Ni−S−H (2.83 mmol g^{-1}, altered secondary coordination sphere), respectively. Experimental and theoretical results indicate that photogenerated electrons are injected from CdS NPs into catalytic Ni(II) sites for H$_2$ generation and support the notion that the modulation of the Ni(II) microenvironment gives rise to different charge transfer dynamics and activation barriers, leading to regulated activity. To the best of our knowledge, this is an unprecedented investigation of the modulation of multiple coordination spheres of catalytic metal sites in MOF-based materials for enhanced photocatalysis.

RESULTS AND DISCUSSION

The UiO-67-type MOF (simply as UiO) with bipyridine chelating sites and its corresponding composite with CdS were prepared according to the previous report to give the CdS/UiO composite (Scheme 1), in which CdS was generated by the reaction between Cd(CH$_3$COO)$_2$·2H$_2$O and dimethyl sulfoxide (DMSO) at high temperature.[36] As observed by scanning electron microscopy (SEM), the MOF morphology does not change upon depositing CdS NPs; the MOF and its resulting composite both present regular octahedra with sizes of ~700 nm (Figure 1a,b). Transmission electron microscopy
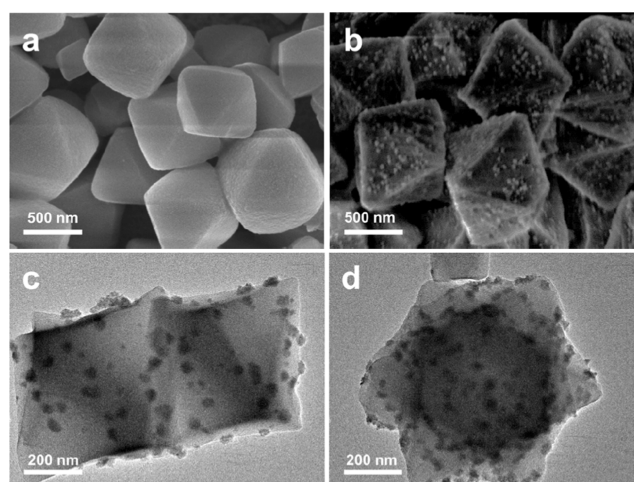

Figure 1. SEM images of (a) the UiO-67-type MOF and (b) its CdS/UiO composite. TEM images of (c) CdS/UiO and (d) CdS/UiO−Ni−S−CF$_3$.

(TEM) images suggest the uniform distribution of CdS NPs (27 ± 0.3 nm) on the external surface of the octahedral MOF crystals (Figures 1c and S1 and S2). By introducing the CdS/UiO composite into a solution of Ni(NO$_3$)$_2$·6H$_2$O to chelate Ni(II), followed by adding and stirring with a solution of coordinated ligands, such as 5-(trifluoromethyl)pyridine-2-thiol (5-CF$_3$PySH), 5-chloropyridine-2-thiol (5-ClPySH), pyridine-2-thiol (PySH) and 5-(trifluoromethyl)pyridine-2-ol (5-CF$_3$PyOH), the resulting CdS/UiO−Ni−X−Y (X = S, O; Y = H, Cl, CF$_3$) composites can be obtained with modulated Ni microenvironment (Scheme 1).[37] Specifically, −SH and −OH groups are utilized to modulate the primary coordination sphere of Ni (X = S or O), while changes in functional groups of ligands (Y = H, Cl, and CF$_3$) are employed to regulate the secondary coordination sphere.

Powder X-ray diffraction (XRD) patterns demonstrate that the crystallinity of the UiO-67-type MOF is well maintained during the postsynthetic modification process (Figure S3). The TEM image further indicates that the postmodification creating modulated Ni microenvironment does not disturb the predeposited CdS NPs (Figure 1d). Inductively coupled plasma atomic emission spectroscopy (ICP-AES) results reveal that the loading amount of Ni in all samples is similar to ~5 wt % (Table S1). Nitrogen sorption isotherms for the post-modified composites reflect a similar feature but lower N$_2$ sorption amounts compared to the CdS/UiO composite (Figure S4), possibly due to the pore space occupation by Ni^{2+} and its corresponding coordinated ligands as well as their mass contribution. In addition, the UV−vis diffuse reflectance spectra suggest that while the UiO-67-type MOF does not give

a visible light response, CdS/UiO shows a remarkable absorption feature in the visible region (Figure 2a). Note-
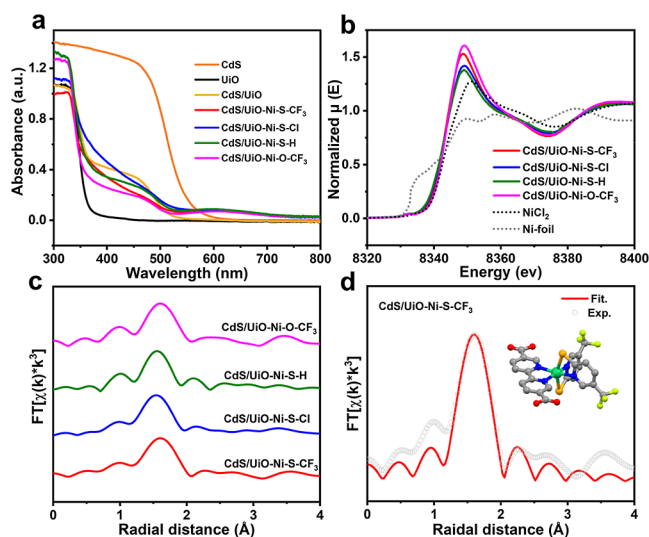
Figure 2. (a) UV−vis diffuse reflectance spectra of CdS, UiO, CdS/UiO, and its corresponding CdS/UiO−Ni−X−Y. (b) Ni K-edge XANES spectra and (c) FT-EXAFS spectra of CdS/UiO−Ni−X−Y. (d) EXAFS fitting of CdS/UiO−Ni−S−CF₃ [inset: proposed structure of Ni(II) site coordinated by 2,2′-bipyridine-5,5′-dicarboxylic acid and 5-(trifluoromethyl)pyridine-2-thiol]. The hydrogen atoms are omitted for clarity (C, gray; S, orange; F, yellow green; N, blue; and Ni, green).

worthily, all CdS/UiO−Ni−X−Y display the characteristic absorption at approximately 600 nm that is attributed to the spin-allowed d−d transition of six-coordinated Ni sites.[38] The ^{1}H NMR spectra of digested CdS/UiO−Ni−X−Y show the peaks of organic linkers and pyridine-2-thiol (or pyridine-2-ol), indicating the presence of the pyridine-2-thiol (or pyridine-2-ol) ligands within the UiO skeleton (Figure S5a). Raman spectra support the existence of Ni−S(O) and Ni−N bonds in the range of 200−500 cm^{-1}, suggesting that S(O) and N atoms in the ligands are coordinated to the Ni sites (Figure S5b).

The X-ray photoelectron spectroscopy (XPS) spectra present the binding energy of 855.6 and 873.3 eV that are assignable to the typical 2p$_{3/2}$ and 2p$_{1/2}$ signals of Ni^{2+}, together with their satellite peaks (Figure S6a), indicating the +2 valence state of Ni species in CdS/UiO−Ni−S−CF₃.[39] In fact, the peaks of Ni 2p$_{3/2}$ and Ni 2p$_{1/2}$ are shifted to higher energies in the following order: CdS/UiO−Ni−O−CF₃ > CdS/UiO−Ni−S−CF₃ > CdS/UiO−Ni−S−Cl > CdS/UiO−Ni−S−H (Figure S6), which is associated with the electronegativity of the primary coordinate atoms and also the electron-withdrawing ability of functional groups on the secondary coordination sphere.

To gain deep insight into the local coordination environment of Ni sites in CdS/UiO−Ni−X−Y composites, steady-state X-ray absorption spectroscopy (XAS) has been examined. The Ni K-edge X-ray absorption near-edge structure (XANES) spectra of all investigated samples show very similar absorption features but are different from those of Ni foil (Figure 2b). Moreover, the differential curves of the Ni K-edge show that the absorption edge of CdS/UiO−Ni−X−Y is very close to that of NiCl₂ (Figure S7), further supporting the +2 oxidation state of Ni species, which is consistent with the above XPS results. Fourier-transformed extended X-ray absorption fine

structure (FT-EXAFS) spectra give one dominant peak at ~1.56 Å ascribed to the Ni−S or Ni−O scattering path, while the Ni−Ni bond at 2.14 Å cannot be observed, confirming the existence of the single Ni^{2+} site (Figures 2c and S8).[33] More importantly, the fitting EXAFS data give more detailed structural information (Figures 2d and S9−S11). For the six-coordinated Ni species in CdS/UiO−Ni−S−CF₃, two 5-(trifluoromethyl)pyridine-2-thiol are chelated to the Ni sites through both N and S atoms on the ligand, whereas the other two Ni−N bonds are formed by the N atoms from the bipyridine-based linker. The Ni−O bond length is shorter than that of Ni−S, which is consistent with the order of the coordinated S and O atom radii (Table S2). The above results manifest the successful synthesis of CdS/UiO−Ni−X−Y.

Photocatalytic H₂ production over CdS/UiO−Ni−X−Y for hydrogen production has been conducted under light irradiation (λ > 380 nm) with lactic acid as the sacrificial agent. Remarkably, the influence of primary and secondary coordination spheres on photocatalytic activity is clearly distinguished. The CdS/UiO−Ni−S−CF₃ exhibits the highest photocatalytic H₂ production rate up to 13.44 mmol g^{-1} in 8 h, followed by CdS/UiO−Ni−S−Cl and CdS/UiO−Ni−S−H with 7.67 and 2.83 mmol g^{-1}, respectively, while it is 0.71 mmol g^{-1} only for CdS/UiO−Ni−O−CF₃ (Figure 3a). As
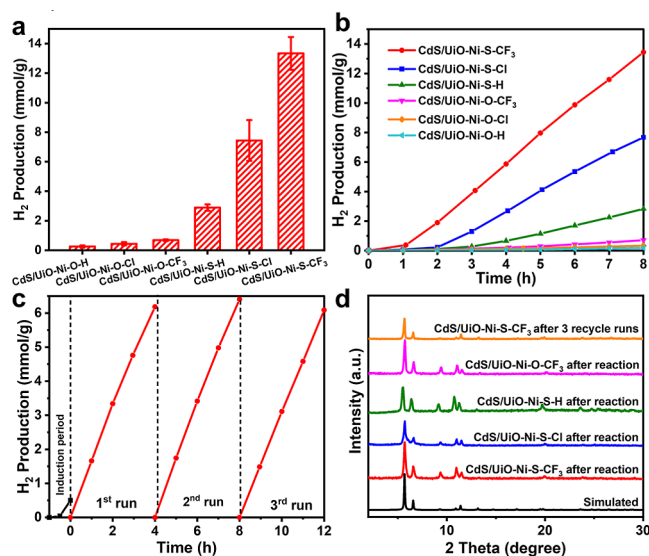
Figure 3. (a) Hydrogen production yield and (b) photocatalytic H₂ production rates of CdS/UiO−Ni−X−Y in 8 h of visible light irradiation. (c) Recycling photocatalytic experiments of CdS/UiO−Ni−S−CF₃. (d) Powder XRD profiles of CdS/UiO−Ni−X−Y after photocatalytic reactions or recycling runs.

light irradiation continues, the amount of hydrogen produced linearly increases, although there is an obvious induction period in the early stage of light irradiation, probably due to the unstable intermediate (Figure 3b).[40,41] The best hydrogen production rate reaches 1.87 mmol g^{-1} h^{-1} when the induction period in the first few hours is not considered. It seems that the primary coordination sphere plays a greater role than the secondary coordination sphere, as indicated by the higher activity of all three catalysts with S atoms than those with O atoms in the primary coordination sphere. For the CdS/UiO−Ni−S−Y photocatalysts with modulated functional groups in the secondary coordination sphere, the hydrogen production rate is closely correlated with the electronic feature of the −Y

group, and the activity follows the trend: CdS/UiO−Ni−S−CF$_3$ > CdS/UiO−Ni−S−Cl > CdS/UiO−Ni−S−H, suggesting that electron-withdrawing substituent can promote activity. In addition, the recycling photocatalytic experiments of CdS/UiO−Ni−S−CF$_3$ show that activity can be maintained in at least three cycles with retained crystallinity (Figure 3c,d), and negligible leaching of Ni and Cd species can be found (Table S1), reflecting the good stability and recyclability of the photocatalyst.

To better clarify the roles of each component in the catalytic system, the photocatalytic performance of the catalysts described above has been investigated. As expected, in the absence of CdS photosensitizer or single Ni sites, the H$_2$ release production rates of 3.6×10^{-4} mmol g^{-1} h^{-1} and 3.7×10^{-3} mmol g^{-1} h^{-1}, respectively, are negligible under identical reaction conditions, indicating that the photosensitizer and catalytic Ni(II) sites are indispensable (Table S3, entries 1−3). The very low H$_2$ release rate of 1.5×10^{-4} mmol g^{-1} h^{-1} is observed with UiO (Table S3, entry 4). Furthermore, the observed poor activity of the physical mixture of CdS and UiO−Ni−S−CF$_3$ in comparison with CdS/UiO−Ni−S−CF$_3$ is due to the possible aggregation of CdS particles (Figure S12 and Table S3, entry 5). The XPS spectra and TEM images have been collected to prove the stable single Ni^{2+} sites in the CdS/UiO−Ni−S−CF$_3$. After the photocatalytic reaction, the characteristic peaks assigned to Ni^{2+} are observed, and no peak corresponding to Ni^0 is detected (Figure S13). Moreover, the substitution of CdS with the classical homogeneous photosensitizer of [Ru(bpy)$_3$]Cl$_2$·6H$_2$O under the same reaction conditions leads to very low activity (Table S3, entry 6) and, meanwhile, no Ni NPs can be observed after the reaction (Figure S14), further reflecting the excellent stability of the Ni species in CdS/UiO−Ni−X−Y catalysts.

To further illuminate the potential electron transfer involved in CdS/UiO−Ni−X−Y, photoelectrochemical measurements have been conducted. The band gaps of CdS and UiO are determined to be 2.36 and 3.58 eV, respectively, by analyzing Tauc plots (Figures S15a and S16a). Mott−Schottky plots provide information on the band positions of CdS and UiO, revealing that their conduction band (CB) positions are −1.30 and −0.80 V vs SCE, respectively (Figures S15b and S16b). This suggests that photoelectrons from CdS are thermodynamically feasible to migrate to UiO. In addition, cyclic voltammetry curves of UiO−Ni−X−Y in organic solvent media have been obtained under an N$_2$ atmosphere. No discernible redox peak can be observed in CH$_3$CN (Figure S17), whereas the reduction peak of Ni^{2+}/Ni$^+$ appears upon the addition of acetic acid in acetonitrile (Figure S18), indicating that the reduction of Ni^{2+} may potentially occur with the assistance of acid, which involves the dissociation of Ni−N bonds.[42,43]

Fundamental insights into charge-separation dynamics can be acquired through femtosecond transient absorption (fs-TA) spectroscopy. The CdS/UiO−Ni−X−Y samples present similar fs-TA spectra upon excitation at 400 nm, including a positive absorption band < 450 nm and a broad negative absorption band > 470 nm (Figures S19−S23). The positive absorption band can be attributed to the stark-effect-induced absorption resulting from the existence of the 1S exciton. The negative feature within the range of 470−500 nm is derived from the 1S exciton bleach. Furthermore, a broad bleach band is observed at wavelengths greater than 600 nm, corresponding to the stimulated emission of CdS.[44−46] The comparison of the

kinetic traces at 490 nm, which reflects the 1S electron lifetime at the CB (Figure 4a), reveals that the presence of single Ni
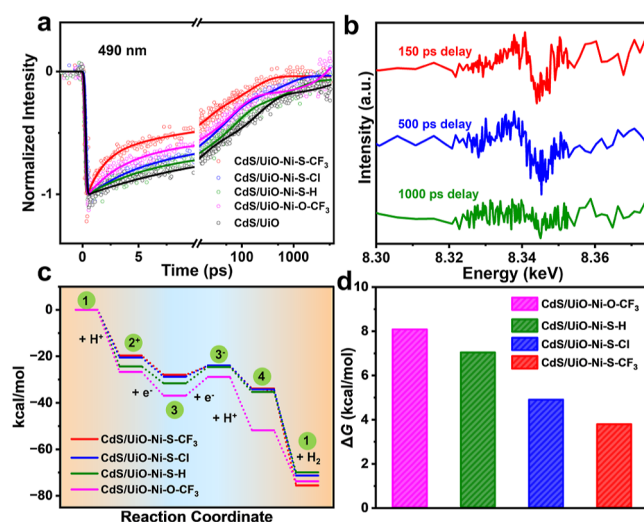
Figure 4. (a) Kinetic profile at 490 nm of transient femtosecond absorption spectra of CdS/UiO−Ni−X−Y upon excitation at 400 nm. (b) XTA difference spectra with 400 nm excitation at time delays of 150, 1000, and 1500 ps on CdS/UiO−Ni−S−CF$_3$. (c) Calculated free energy diagrams of hydrogen production over CdS/UiO−Ni−X−Y. (d) Energy barrier of the second electron transfer to the Ni sites over different photocatalysts.

sites can facilitate electron transfer from CdS to the Ni sites, and the lifetime of CdS/UiO−Ni−S−Y follows the order: CdS/UiO−Ni−S−CF$_3$ (140 ps) < CdS/UiO−Ni−S−Cl (604 ps) < CdS/UiO−Ni−S−H (978 ps). This is consistent with the capability of the electron-withdrawing group in the secondary coordination sphere and suggests that electron transfer from 1S CB of CdS to the catalytic Ni center is faster in the photocatalyst with the stronger electron-withdrawing group. Moreover, CdS/UiO−Ni−O−CF$_3$ displays a slightly longer lifetime than CdS/UiO−Ni−S−CF$_3$, suggesting that in addition to the secondary coordination sphere, the primary coordination sphere also alters the driving force of electron transfer from CdS to the Ni sites. X-ray transient absorption (XTA) spectra at different delay times have been monitored for tracking the valence change of nickel following 400 nm excitation (Figure 4b). At the time delays at 150, 500, and 1000 ps, a prominent positive transient signal at edge energy 8.337 keV is observed, which suggests an edge shift to lower energy (Figure 4b), indicating the reduction of Ni^{2+} to Ni$^+$ upon photoexcitation of CdS, and unambiguously confirms electron transfer process from CdS to Ni center.[47]

Given the aforementioned observations and previous reports,[38] a reasonable photocatalytic cycle for proton reduction has been proposed (Figure S24). The reaction initiates with protonation of the pyridyl nitrogen, while simultaneous dechelation occurs between the N and Ni atoms (intermediate 2$^+$ in Figure S24). Upon light irradiation, the Ni(II) species undergoes subsequent reduction through electron transfer from the photosensitizer CdS (intermediate 3 in Figure S24). Then, the active nickel-hydride intermediate is generated on account of the second protonation and electron transfer (intermediate 4 in Figure S24). Finally, H$^+$ from the protonated pyridyl group combines with the proposed Ni(II)−H intermediate to release H$_2$ during the catalytic cycle.

To better understand the impact of the coordination sphere of single Ni sites on photocatalytic hydrogen production, density functional theory (DFT) calculations have been adopted.[48,49] Four computational models are constructed based on the key part involving catalytic Ni(II) site and its microenvironment (Figures S25−S28), with each reaction intermediate species optimized for calculating their relative free energy (Tables S4−S7). The free energy diagram shows that, in the catalytic cycle, except for the formation of nickel-hydride intermediates (intermediate 4 in Figures 4c and S24), the energies of the catalytic intermediates gradually decrease from the energy of catalyst protonation, first electron transfer, and the release of hydrogen, suggesting that the rate-determining step (RDS) is the second protonation and electron transfer process (Figures 4c and S24 and Table S8). As expected, CdS/UiO−Ni−S−CF$_3$ exhibits the lowest Gibbs free energy barrier (ΔG) among all of the catalysts, indicating that the single Ni(II) site with the S atom on the primary coordination sphere and −CF$_3$ on the secondary coordination sphere is favorable for photocatalytic H$_2$ production. Furthermore, the order of ΔG for the second electron transfer to Ni sites in CdS/UiO−Ni−X−Y is as follows: CdS/UiO−Ni−S−CF$_3$ (ΔG = 3.77 kcal mol^{-1}) < CdS/UiO−Ni−S−Cl (ΔG = 4.87 kcal mol^{-1}) < CdS/UiO−Ni−S−H (ΔG = 7.02 kcal mol^{-1}) < CdS/UiO−Ni−O−CF$_3$ (ΔG = 8.07 kcal mol^{-1}), which is consistent with the observed experimental activity trend (Figure 4d and Table S8). Note that the change in coordinated atoms on the primary coordination sphere is the paramount determinant of catalytic performance when comparing the ΔG of the RDS and charge-separation dynamics. If the analysis focuses solely on the changes in the secondary coordination sphere, it becomes apparent that the energy barrier, charge-separation kinetics, and activity are compatible, demonstrating the catalytic performance can be further optimized by modulating the second coordination sphere based on the defined primary coordination sphere.

CONCLUSIONS

In conclusion, we have constructed a series of MOF-based single-site Ni catalysts, namely, UiO−Ni−X−Y, featuring modulated primary and secondary coordination spheres of Ni(II) sites for photocatalytic H$_2$ production, in the presence of CdS as the photosensitizer. Strikingly, among CdS/UiO−Ni−X−Y photocatalysts, CdS/UiO−Ni−S−CF$_3$ exhibits the highest photocatalytic hydrogen production rate of 1.87 mmol g^{-1} h^{-1}, far surpassing all other counterparts, namely CdS/UiO−Ni−S−Cl (1.06 mmol g^{-1} h^{-1}), CdS/UiO−Ni−S−H (0.51 mmol g^{-1} h^{-1}), and CdS/UiO−Ni−O−CF$_3$ (0.11 mmol g^{-1} h^{-1}). Both primary coordinated atoms and the functional groups in the secondary coordination sphere are found to play critical roles in regulating the charge separation dynamics and energy barrier of the RDS. Specifically, the results of fs-TA spectra suggest that electron transfer is influenced by the microenvironment of catalytic Ni sites, where the primary coordination sphere exerts a more significant impact compared to the secondary coordination sphere. This work emphasizes the importance of modulating the coordination microenvironment around catalytic metal sites in photocatalysis, which would provide significant inspiration and guidance in the design and synthesis of heterogeneous catalysts in the future.

MATERIALS AND METHODS

Materials and Equipment. All chemicals were purchased from commercial sources and used without further treatment. Powder XRD patterns were measured on a Japan Rigaku Miniflex 600 rotation anode X-ray diffractometer equipped with graphite-monochromatized Cu Kα radiation (λ = 1.54 Å). Field-emission SEM was carried out with a field-emission scanning electron microanalyzer (Zeiss Supra 40 scanning electron microscope at an acceleration voltage of 5 kV). The size and morphology of samples were investigated by TEM on JEOL-2010 instruments with an electron acceleration energy of 200 kV. ICP-AES with an Optima 7300 DV was adopted for quantitative analysis of the contents of Ni. Nitrogen sorption measurements were conducted using automatic volumetric adsorption equipment Micromeritics ASAP 2020 at 77 K. The ^{1}H NMR spectra were performed on a nuclear magnetic resonance spectrometer (Bruker AVANCE AV III 400). UV−vis diffuse reflectance spectra were recorded on a Shimadzu UV-2700 using a white standard of BaSO$_4$ as a reference. Raman spectra were collected on the Horiba LabRAM SoLeil Confocal Raman System with a 785 nm laser. Electrochemical characterizations were characterized with a Zahner Zennium electrochemical workstation or CHI 760E electrochemical workstation (Chenhua Instrument, Shanghai, China). XPS measurements were performed with an ESCALAB 250 high-performance electron spectrometer using monochromated Al Kα radiation ($h\nu$ = 1486.7 eV) as the excitation source. The catalytic reaction product H$_2$ was analyzed and identified by gas chromatography (Shimadzu GC-2014).

Synthesis of UiO-67 Type MOF. Typically, 73.5 mg of ZrCl$_4$, 78 mg of 2,2-bipyridine-5,5-dicarboxylic acid (bpydc), and 3 mL of formic acid (HCOOH) were ultrasonically dispersed in 30 mL of DMF. Subsequently, the mixed solution was sealed into an 80 mL vessel and heated at 120 °C for 24 h. The as-synthesized UiO-bpy was filtered, washed with DMF and EtOH, and then dried at 60 °C under vacuum to obtain white powder (yield: 72%).

Synthesis of CdS/UiO. The CdS NPs were successfully decorated on the surface of UiO by high-temperature vulcanization. Generally, 150 mg of as-synthesized UiO and 15 mg of Cd(CH$_3$COO)$_2$·2H$_2$O were ultrasonically dispersed in 40 mL of DMSO for stirring for a couple of hours, and then the mixture was sealed into a Teflon-lined stainless steel autoclave and kept at 180 °C for 10 h. After cooling down to room temperature, the harvested yellow sample was washed with water and ethanol several times and further dried at 60 °C under vacuum to yield CdS/UiO.

Synthesis of CdS/UiO−Ni−X−Y. In the experiment, CdS/UiO (50 mg) was added to a CH$_3$CN solution of Ni(NO$_3$)$_2$·(H$_2$O)$_6$. The suspension was slowly stirred for a certain period of time. The green solid was then filtrated, washed with CH$_3$CN, and dried. The resulting powder was redispersed in acetonitrile. A solution containing coordinated ligand (1 equiv), such as 5-CF$_3$PySH, 5-ClPySH, PySH, or 5-CF$_3$PyOH, and triethylamine (1.25 equiv) in CH$_3$CN was dropwise added to the above mixture. After stirring for another few hours, the obtained product was collected by filtration and washed with CH$_3$CN, finally dried under a vacuum.

Synthesis of UiO−Ni−X−Y. The UiO−Ni−X−Y was synthesized following the same procedure as that for CdS/UiO−Ni−X−Y except UiO was used only.

Synthesis of CdS. Typically, the ethanol (10 mL) solution of Cd(CH$_3$COO)$_2$·2H$_2$O (92 mg) was heated at 80 °C for 10 min. Then, thioacetamide (26 mg) in H$_2$O (10 mL) was injected into the flask slowly, stirred vigorously, and maintained at 80 °C for 30 min. The precipitates were filtered and rinsed with H$_2$O and ethanol several times and finally dried at 60 °C under vacuum.

Electrochemical Measurements. The cyclic voltammetry measurements were conducted using a CHI 760E electrochemical workstation (Chenhua Instrument, Shanghai, China) with a standard three-electrode system in CH$_3$CN with 0.1 M tetrabutylammonium fluoride under a nitrogen atmosphere. The working electrode was the catalyst-coated glassy carbon (Φ = 3 cm), while the Pt plate was used as the counter electrode and Ag/Ag$^+$ as the reference electrode. Ferrocene was used as an internal standard in organic electrolytes to

correct potentials. Generally, 3 mg of catalyst was dispersed into 2 mL of sodium alginate aqueous solution (0.1 mg/mL). Then, the suspension (20 μL) was dropped onto the surface of the working electrode and waited for air drying. Mott–Schottky measurements were performed using a Zahner Zennium electrochemical workstation with a conventional three-electrode cell in 0.1 M Na_2SO_4 solution at frequencies of 500, 1000, and 1500 Hz, respectively. The catalyst-coated glassy carbon electrode (Φ = 3 cm) was utilized as the working electrode, with a Pt plate serving as the counter electrode and Ag/AgCl as the reference electrode. Typically, 3 mg of catalyst was dispersed into the solution containing 0.3 mL of ethanol and 10 μL of 5 wt % Nafion. The working electrode was prepared by dropping the suspension (50 μL) onto the surface of glassy carbon and waiting it for air drying.

Steady-State XAS Measurements. XAS measurements were conducted at the 12-BM-B beamline at the Advanced Photon Source of Argonne National Laboratory. The XAS data were collected in fluorescence mode at room temperature. During the measurements, the prepared samples are covered with Kapton tape and placed onto the sample holder. Nickel foil is used for energy calibration. The XANES and EXAFS data were analyzed using the Athena and Artemis packages based on FEFF programs.

XTA Measurements. The XTA data were obtained at beamline 11-ID-D at the Advanced Photon Source of Argonne National Laboratory. To prepare the samples for XTA measurements, the catalyst was dispersed into a mixture of acetonitrile, lactic acid, and water to make a suspension. The suspensions are transferred to the XTA glass cell and irradiated with a 400 nm laser in the laser-on experiment. The laser-on and laser-off spectra are collected at 150, 500, and 1000 ps, respectively, after the sample suspension is excited by a 400 nm laser pump pulse. The difference spectrum is acquired by extracting the difference between the laser-on and laser-off spectra.

Ultrafast Spectroscopy Measurements. fs-TA spectroscopy was collected in a Helios ultrafast spectrometer with pump and probe pulses resulting from a regenerative amplified Ti-sapphire laser system (Solstice, 800 nm, <100 fs FWHM, 3.5 mJ/pulse, 1 kHz repetition rate). To prepare the thin film samples for fs-TA measurements, 1 mg of catalyst was added into a glass vial containing 0.5 mL of Nafion (5% w/w in water and 1-propanol). The resulting mixture was stirred for a certain time before being uniformly distributed onto a piranha-etched glass slide. The samples were subsequently air-dried to obtain the film that was continuously translated during the fs-TA experiment to prevent heating and permanent degradation. For all measurements, the pump power is 0.5 mW under 400 nm excitation.

General Photocatalytic Procedure for H$_2$ Production. The experiment was carried out in a 160 mL optical reaction vessel with stirring at ambient temperature using a 300 W xenon lamp (LX-300F, Japan) with a UV cutoff filter (λ > 380 nm). Typically, 10 mg of sample was dispersed in 20 mL of acetonitrile and 0.4 mL of deionized water with 2 mL of lactic acid as the sacrificial reagent, and then the mixture was purged with nitrogen for 15 min to completely remove air. The reaction was driven under light irradiation using an Xe lamp and mechanical stirring while maintaining the reaction temperature through circulating water. After the reaction, the gas products were analyzed by GC using a thermal conductivity detector (TCD) and quantified by a calibration plot to the internal hydrogen standard.

Recycling Performance of Photocatalytic H$_2$ Production. After completion of each catalytic cycle, the catalyst should be handled with care to avoid its weight loss during the centrifugation between each two catalytic runs and immediately redispersed in the reaction solution for the next run under light irradiation. The photocatalytic activity of H$_2$ production was analyzed by GC-TCD.

Computational Details. The DFT calculations were performed using the quantum chemistry package Gaussian 16.[50] The geometry optimization and frequency calculations of the catalysts used the PBE0 functional with def-tzvp basis sets.[51,52] To obtain the single-point energy of each intermediate, the same function with the def2-tzvp basis set was utilized. Moreover, all calculations were carried out with an implicit solvent model with a dielectric constant simulating the experimental solvent environment, in which Grimme's D3BJ dispersion correction was implemented for all structures.[53] According to the catalytic process, Gaussian 16 was implemented to build the most reasonable intermediate models. Considering the geometrical structures with a spin state of 3 and optimized structures based on DFT,[38] the corresponding complex geometries, spin states, and Gibbs energies of each intermediate were determined. The related structural parameters, including bond lengths and bond angles, were obtained using GaussView 6.0 visualization software.

ASSOCIATED CONTENT

Ⓢ Supporting Information

The Supporting Information is available free of charge at https://pubs.acs.org/doi/10.1021/jacs.4c00972.

Details on ligand preparation, characterization data and figures (PDF)

AUTHOR INFORMATION

Corresponding Authors

Jier Huang — Department of Chemistry and Schiller Institute for Integrated Science and Society, Boston College, Chestnut Hill, Massachusetts 02467, United States; Ⓞ orcid.org/0000-0002-2885-5786; Email: jier.huang@bc.edu

Hai-Long Jiang — Hefei National Research Center for Physical Sciences at the Microscale, Department of Chemistry, University of Science and Technology of China, Hefei, Anhui 230026, P. R. China; Ⓞ orcid.org/0000-0002-2975-7977; Email: jianglab@ustc.edu.cn

Authors

Ge Yang — Hefei National Research Center for Physical Sciences at the Microscale, Department of Chemistry, University of Science and Technology of China, Hefei, Anhui 230026, P. R. China

Denan Wang — Department of Chemistry and Schiller Institute for Integrated Science and Society, Boston College, Chestnut Hill, Massachusetts 02467, United States; Ⓞ orcid.org/0000-0003-3603-6788

Yang Wang — Key Laboratory of Precision and Intelligent Chemistry, School of Chemistry and Materials Science, University of Science and Technology of China, Hefei, Anhui 230026, P. R. China

Wenhui Hu — Department of Chemistry, Marquette University, Milwaukee, Wisconsin 53201, United States

Shuaishuai Hu — Hefei National Research Center for Physical Sciences at the Microscale, Department of Chemistry, University of Science and Technology of China, Hefei, Anhui 230026, P. R. China

Jun Jiang — Key Laboratory of Precision and Intelligent Chemistry, School of Chemistry and Materials Science, University of Science and Technology of China, Hefei, Anhui 230026, P. R. China; Ⓞ orcid.org/0000-0002-6116-5605

Complete contact information is available at:
https://pubs.acs.org/10.1021/jacs.4c00972

Author Contributions

$^{\perp}$G.Y., D.W., and Y.W. contributed equally.

Notes

The authors declare no competing financial interest.

■ REFERENCES

(1) Tao, X.; Zhao, Y.; Wang, S.; Li, C.; Li, R. Recent advances and perspectives for solar-driven water splitting using particulate photocatalysts. *Chem. Soc. Rev.* **2022**, *51*, 3561−3608.

(2) Wang, Z.; Li, C.; Domen, K. Recent developments in heterogeneous photocatalysts for solar-driven overall water splitting. *Chem. Soc. Rev.* **2019**, *48*, 2109−2125.

(3) Song, H.; Luo, S.; Huang, H.; Deng, B.; Ye, J. Solar-driven hydrogen production: recent advances, challenges, and future perspectives. *ACS Energy Lett.* **2022**, *7*, 1043−1065.

(4) Zhou, P.; Navid, I. A.; Ma, Y.; Xiao, Y.; Wang, P.; Ye, Z.; Zhou, B.; Sun, K.; Mi, Z. Solar-to-hydrogen efficiency of more than 9% in photocatalytic water splitting. *Nature* **2023**, *613*, 66−70.

(5) Wang, Q.; Pornrungroj, C.; Linley, S.; Reisner, E. Strategies to improve light utilization in solar fuel synthesis. *Nat. Energy* **2022**, *7*, 13−24.

(6) Chen, F.; Ma, T.; Zhang, T.; Zhang, Y.; Huang, H. Atomic-level charge separation strategies in semiconductor-based photocatalysts. *Adv. Mater.* **2021**, *33*, 2005256.

(7) Liu, L.; Du, S.; Guo, X.; Xiao, Y.; Yin, Z.; Yang, N.; Bao, Y.; Zhu, X.; Jin, S.; Feng, Z.; Zhang, F. Water-stable nickel metal-organic framework nanobelts for cocatalyst-free photocatalytic water splitting to produce hydrogen. *J. Am. Chem. Soc.* **2022**, *144*, 2747−2754.

(8) Jia, G.; Sun, M.; Wang, Y.; Cui, X.; Huang, B.; Yu, J. C. Enabling efficient photocatalytic hydrogen evolution via in situ loading of Ni single atomic sites on red phosphorus quantum dots. *Adv. Funct. Mater.* **2023**, *33*, 2212051.

(9) Tang, H.; Hall, M. B. Biomimetics of [NiFe]-hydrogenase: nickel- or iron-centered proton reduction catalysis? *J. Am. Chem. Soc.* **2017**, *139*, 18065−18070.

(10) Benkovic, S. J.; Hammes-Schiffer, S. A perspective on enzyme catalysis. *Science* **2003**, *301*, 1196−1202.

(11) Fu, Q.; Bao, X. Confined microenvironment for catalysis control. *Nat. Catal.* **2019**, *2*, 834−836.

(12) López-Alonso, J. P.; Lázaro, M.; Gil-Cartón, D.; Choi, P. H.; Dodu, A.; Tong, L.; Valle, M. CryoEM structural exploration of catalytically active enzyme pyruvate carboxylase. *Nat. Commun.* **2022**, *13*, 6185.

(13) Gong, Y.-N.; Cao, C.-Y.; Shi, W.-J.; Zhang, J.-H.; Deng, J.-H.; Lu, T.-B.; Zhong, D.-C. Modulating the electronic structures of dual-atom catalysts via coordination environment engineering for boosting CO₂ electroreduction. *Angew. Chem.* **2022**, *134*, No. e202215187.

(14) Tang, C.; Jiao, Y.; Shi, B.; Liu, J.-N.; Xie, Z.; Chen, X.; Zhang, Q.; Qiao, S.-Z. Coordination tunes selectivity: two-electron oxygen reduction on high-loading molybdenum single-atom catalysts. *Angew. Chem., Int. Ed.* **2020**, *59*, 9171−9176.

(15) Zhang, Y.; Dong, L.-Z.; Li, S.; Huang, X.; Chang, J.-N.; Wang, J.-H.; Zhou, J.; Li, S.-L.; Lan, Y.-Q. Coordination environment dependent selectivity of single-site-Cu enriched crystalline porous catalysts in CO₂ reduction to CH₄. *Nat. Commun.* **2021**, *12*, 6390.

(16) Gao, Y.; Liu, B.; Wang, D. Microenvironment engineering of single/dual-atom catalysts for electrocatalytic application. *Adv. Mater.* **2023**, *35*, 2209654.

(17) Teindl, K.; Patrick, B. O.; Nichols, E. M. Linear free energy relationships and transition state analysis of CO₂ reduction catalysts bearing second coordination spheres with tunable acidity. *J. Am. Chem. Soc.* **2023**, *145*, 17176−17186.

(18) Liu, M.; Li, N.; Wang, X.; Zhao, J.; Zhong, D.-C.; Li, W.; Bu, X.-H. Photosystem II inspired NiFe-based electrocatalysts for efficient water oxidation via second coordination sphere effect. *Angew. Chem.* **2023**, *135*, No. e202300507.

(19) Stripp, S. T.; Duffus, B. R.; Fourmond, V.; Léger, C.; Leimkühler, S.; Hirota, S.; Hu, Y.; Jasniewski, A.; Ogata, H.; Ribbe, M. W. Second and outer coordination sphere effects in nitrogenase, hydrogenase, formate dehydrogenase, and CO dehydrogenase. *Chem. Rev.* **2022**, *122*, 11900−11973.

(20) Riscoe, A. R.; Wrasman, C. J.; Herzing, A. A.; Hoffman, A. S.; Menon, A.; Boubnov, A.; Vargas, M.; Bare, S. R.; Cargnello, M. Transition state and product diffusion control by polymer-nanocrystal hybrid catalysts. *Nat. Catal.* **2019**, *2*, 852−863.

(21) Dong, K.; Sun, Q.; Tang, Y.; Shan, C.; Aguila, B.; Wang, S.; Meng, X.; Ma, S.; Xiao, F.-S. Bio-inspired creation of heterogeneous reaction vessels via polymerization of supramolecular ion pair. *Nat. Commun.* **2019**, *10*, 3059.

(22) Furukawa, H.; Cordova, K. E.; O'Keeffe, M.; Yaghi, O. M. The chemistry and applications of metal-organic frameworks. *Science* **2013**, *341*, 1230444.

(23) Horike, S.; Kitagawa, S. The development of molecule-based porous material families and their future prospects. *Nat. Mater.* **2022**, *21*, 983−985.

(24) Liu, J.; Goetjen, T. A.; Wang, Q.; Knapp, J. G.; Wasson, M. C.; Yang, Y.; Syed, Z. H.; Delferro, M.; Notestein, J. M.; Farha, O. K.; Hupp, J. T. MOF-enabled confinement and related effects for chemical catalyst presentation and utilization. *Chem. Soc. Rev.* **2022**, *51*, 1045−1097.

(25) Zhao, X.; Wang, Y.; Li, D. S.; Bu, X.; Feng, P. Metal-organic frameworks for separation. *Adv. Mater.* **2018**, *30*, 1705189.

(26) Kirchon, A.; Feng, L.; Drake, H. F.; Joseph, E. A.; Zhou, H.-C. From fundamentals to applications: a toolbox for robust and multifunctional MOF materials. *Chem. Soc. Rev.* **2018**, *47*, 8611−8638.

(27) Jiao, L.; Wang, J.; Jiang, H.-L. Microenvironment modulation in metal-organic framework-based catalysis. *Acc. Mater. Res.* **2021**, *2*, 327−339.

(28) Huang, N.-Y.; Shen, J.-Q.; Zhang, X.-W.; Liao, P.-Q.; Zhang, J.-P.; Chen, X.-M. Coupling ruthenium bipyridyl and cobalt imidazolate units in a metal-organic framework for an efficient photosynthetic overall reaction in diluted CO₂. *J. Am. Chem. Soc.* **2022**, *144*, 8676−8682.

(29) Zhuo, T.-C.; Song, Y.; Zhuang, G.-L.; Chang, L.-P.; Yao, S.; Zhang, W.; Wang, Y.; Wang, P.; Lin, W.; Lu, T.-B.; Zhang, Z.-M. H-Bond-Mediated Selectivity Control of Formate versus CO during CO₂ Photoreduction with Two Cooperative Cu/X Sites. *J. Am. Chem. Soc.* **2021**, *143*, 6114−6122.

(30) Stanley, P. M.; Haimerl, J.; Shustova, N. B.; Fischer, R. A.; Warnan, J. Merging molecular catalysts and metal-organic frameworks for photocatalytic fuel production. *Nat. Chem.* **2022**, *14*, 1342−1356.

(31) Navalón, S.; Dhakshinamoorthy, A.; Alvaro, M.; Ferrer, B.; Garcia, H. Metal-organic frameworks as photocatalysts for solar-driven overall water splitting. *Chem. Rev.* **2023**, *123*, 445−490.

(32) Guo, J.; Qin, Y.; Zhu, Y.; Zhang, X.; Long, C.; Zhao, M.; Tang, Z. Metal-organic frameworks as catalytic selectivity regulators for organic transformations. *Chem. Soc. Rev.* **2021**, *50*, 5366−5396.

(33) Ma, X.; Liu, H.; Yang, W.; Mao, G.; Zheng, L.; Jiang, H.-L. Modulating Coordination Environment of Single-Atom Catalysts and Their Proximity to Photosensitive Units for Boosting MOF Photocatalysis. *J. Am. Chem. Soc.* **2021**, *143*, 12220−12229.

(34) Wang, J.; Sun, K.; Wang, D.; Niu, Xi.; Lin, Z.; Wang, S.; Yang, W.; Huang, J.; Jiang, H.-L. Precise regulation of the coordination

environment of single Co(II) sites in a metal-organic framework for boosting CO2 photoreduction. *ACS Catal.* **2023**, *13*, 8760−8769.

(35) Guo, Y.; Wang, Y.; Shen, Y.; Cai, Z.; Li, Z.; Liu, J.; Chen, J.; Xiao, C.; Liu, H.; Lin, W.; Wang, C. Tunable cobalt-polypyridyl catalysts supported on metal-organic layers for electrochemical CO_2 reduction at low overpotentials. *J. Am. Chem. Soc.* **2020**, *142*, 21493−21501.

(36) Chen, C.; Wu, T.; Wu, H.; Liu, H.; Qian, Q.; Liu, Z.; Yang, G.; Han, B. Highly effective photoreduction of CO_2 to CO promoted by integration of CdS with molecular redox catalysts through metal-organic frameworks. *Chem. Sci.* **2018**, *9*, 8890−8894.

(37) Lee, S. E.; Nasirian, A.; Kim, Y. E.; Fard, P. T.; Kim, Y.; Jeong, B.; Kim, S.-J.; Baeg, J.-O.; Kim, J. Visible-light photocatalytic conversion of carbon dioxide by Ni(II) complexes with N_4S_2 coordination: highly efficient and selective production of formate. *J. Am. Chem. Soc.* **2020**, *142*, 19142−19149.

(38) Han, Z.; Shen, L.; Brennessel, W. W.; Holland, P. L.; Eisenberg, R. Nickel pyridinethiolate complexes as catalysts for the light-driven production of hydrogen from aqueous solutions in noble-metal free systems. *J. Am. Chem. Soc.* **2013**, *135*, 14659−14669.

(39) Yan, Z.-H.; Ma, B.; Li, S.-R.; Liu, J.; Chen, R.; Du, M.-H.; Jin, S.; Zhuang, G.-L.; Long, L.-S.; Kong, X.-J.; Zheng, L.-S. Encapsulating a Ni(II) molecular catalyst in photoactive metal-organic framework for highly efficient photoreduction of CO_2. *Sci. Bull.* **2019**, *64*, 976−985.

(40) Huang, J.; Mulfort, K. L.; Du, P.; Chen, L. X. Photodriven charge separation dynamics in CdSe/ZnS core/shell quantum dot/cobaloxime hybrid for efficient hydrogen production. *J. Am. Chem. Soc.* **2012**, *134*, 16472−16475.

(41) Rahman, M.; Tian, H.; Edvinsson, T. Revisiting the limiting factors for overall water-Splitting on organic photocatalysts. *Angew. Chem.* **2020**, *132*, 16418−16433.

(42) Wang, J.-W.; Liu, W.-J.; Zhong, D.-C.; Lu, T.-B. Nickel complexes as molecular catalysts for water splitting and CO_2 reduction. *Coord. Chem. Rev.* **2019**, *378*, 237−261.

(43) Han, Z.; McNamara, W. R.; Eum, M. S.; Holland, P. L.; Eisenberg, R. A nickel thiolate catalyst for the long-lived photocatalytic production of hydrogen in a noble-metal-free system. *Angew. Chem., Int. Ed.* **2012**, *51*, 1667−1670.

(44) Wang, F.; Hou, T.; Zhao, X.; Yao, W.; Fang, R.; Shen, K.; Li, Y. Ordered macroporous carbonous frameworks implanted with CdS quantum dots for efficient photocatalytic CO_2 reduction. *Adv. Mater.* **2021**, *33*, 2102690.

(45) Zhu, Q.; Xu, Q.; Du, M.; Zeng, X.; Zhong, G.; Qiu, B.; Zhang, J. Recent progress of metal sulfide photocatalysts for solar energy conversion. *Adv. Mater.* **2022**, *34*, 2202929.

(46) Wang, D.; Hu, W.; Reinhart, B. J.; Zhang, X.; Huang, J. Tuning the charge transport property and photocatalytic activity of anthracene-based 1D π-d conjugated coordination polymers by interlayer stacking. *ACS Appl. Mater. Interfaces* **2022**, *14*, 42171−42177.

(47) Nyakuchena, J.; Zhang, X.; Huang, J. Synchrotron based transient X-ray absorption spectroscopy for emerging solid-state energy materials. *Chem. Phys. Rev.* **2023**, *4*, 021303.

(48) Samanta, B.; Morales-García, Á.; Illas, F.; Goga, N.; Anta, J. A.; Calero, S.; Bieberle-Hütter, A.; Libisch, F.; Muñoz-García, A. B.; Pavone, M.; Caspary Toroker, M. Challenges of modeling nanostructured materials for photocatalytic water splitting. *Chem. Soc. Rev.* **2022**, *51*, 3794−3818.

(49) Sun, F.; Tang, Q.; Jiang, D.-e. Theoretical advances in understanding and designing the active sites for hydrogen evolution reaction. *ACS Catal.* **2022**, *12*, 8404−8433.

(50) Frisch, M. J.; Trucks, G. W.; Schlegel, H. B.; Scuseria, G. E.; Robb, M. A.; Cheeseman, J. R.; Scalmani, G.; Barone, V.; Petersson, G. A.; Nakatsuji, H.; Li, X.; Caricato, M.; Marenich, A. V.; Bloino, J.; Janesko, B. G.; Gomperts, R.; Mennucci, B.; Hratchian, H. P.; Ortiz, J. V.; Izmaylov, A. F.; Sonnenberg, J. L.; Williams, F. D.; Lipparini, F.; Egidi, F.; Goings, J.; Peng, B.; Petrone, A.; Henderson, T.; Ranasinghe, D.; Zakrzewski, V. G.; Gao, J.; Rega, N.; Zheng, G.; Liang, W.; Hada, M.; Ehara, M.; Toyota, K.; Fukuda, R.; Hasegawa, J.; Ishida, M.; Nakajima, T.; Honda, Y.; Kitao, O.; Nakai, H.; Vreven, T.; Throssell, K.; Montgomery, J. A., Jr.; Peralta, J. E.; Ogliaro, F.; Bearpark, M. J.; Heyd, J. J.; Brothers, E. N.; Kudin, K. N.; Staroverov, V. N.; Keith, T. A.; Kobayashi, R.; Normand, J.; Raghavachari, K.; Rendell, A. P.; Burant, J. C.; Iyengar, S. S.; Tomasi, J.; Cossi, M.; Millam, J. M.; Klene, M.; Adamo, C.; Cammi, R.; Ochterski, J. W.; Martin, R. L.; Morokuma, K.; Farkas, O.; Foresman, J. B.; Fox, D. J. *Gaussian 16 A.03*; Gaussian, Inc.: Wallingford, CT, 2016.

(51) Adamo, C.; Barone, V. Toward reliable density functional methods without adjustable parameters: the PBE0 model. *J. Chem. Phys.* **1999**, *110*, 6158−6170.

(52) Schäfer, A.; Horn, H.; Ahlrichs, R. Fully optimized contracted Gaussian basis sets for atoms Li to Kr. *J. Chem. Phys.* **1992**, *97*, 2571−2577.

(53) Grimme, S.; Antony, J.; Ehrlich, S.; Krieg, H. A consistent and accurate ab initio parametrization of density functional dispersion correction (DFT-D) for the 94 elements H-Pu. *J. Chem. Phys.* **2010**, *132*, 154104.